



Comparative analysis of Edge Detection techniques for SAR images

Felix Bachofer^{1*}, Geraldine Quénéhervé¹, Thimm Zwiener¹,
Michael Maerker^{2,3} and Volker Hochschild¹

¹Institute of Geography, University of Tuebingen, Ruemelinstr, 19, D-72070 Tuebingen, Germany

²Heidelberg Academy of Sciences and Humanities, Ruemelinstr, 23, D-72070 Tuebingen, Germany

³Earth Science Department, University of Florence, Via G. La Pira 4, I-50121 Florence, Italy

*Corresponding author, e-mail address: felix.bachofer@uni-tuebingen.de

Abstract

Paleo-shorelines and ancient lake terraces east of Lake Manyara in Tanzania were identified from the backscatter intensity of TerraSAR-X StripMap images. Because of their linear alignment, edge detector algorithms were applied to delineate these morphological structures from those Synthetic Aperture Radar scenes. Due to the physical properties of microwave signals, this application has proven to be a challenging task for edge detectors. This study compares the performance of different combinations of speckle reduction techniques and edge operator in detecting linear paleo-shorelines. The Roberts, Sobel, Laplacian of Gaussian and the Canny edge detector algorithms were applied to extract and revise those linear structures. The comparison shows that the Canny edge detector is especially suitable for images with strong speckle noise. Canny achieves relatively high accuracies compared to the other operators. The stronger the filtering and speckle noise reduction, the better the performance of the other edge detection operators, compared to the Canny edge detector. The application of a wavelet transformation reduces the presence of artifacts resulting from speckle noise and emphasizes the detection of the target features.

Keywords: Edge operators, SAR data, speckle noise, TerraSAR-X, Wavelet Transformation.

Introduction

This study provides a comparison of different pre-processing and edge detection techniques. The set-up of the proposed work is a research project located in the Gregory Rift, east of Lake Manyara in northern Tanzania. The study area is characterized by paleo-shorelines which are related to different paleolake levels. Those linear structures appear mainly in the form of terraces and beaches. The geomorphological features and forms have been mapped only to a small extent, while some were investigated further with radiometric dating methods [Keller et al., 1975; Casanova and Hillaire-Marcel, 1992; Somi, 1993]. Optical remote sensing methods failed to delineate the above mentioned paleolake features due to spectral similarities with the surface in the vicinity. Hence, we utilized the backscatter intensity information from TerraSAR-X StripMap [Bachofer et al., 2014]. The

morphological structures of shorelines and terraces east of Lake Manyara are characterized by high Synthetic Aperture Radar (SAR) backscatter values, due to their distinct geometric structure and texture (high share of gravel).

Remote sensing analysis in paleo-landscape research is a widely used and accepted method. The combination of satellite image data with digital elevation models (DEM) was applied to delineate paleolakes and paleolake related features [Ghoneim and El-Baz, 2007; Gaber et al., 2009; Elmahdy, 2012; Bachofer et al., 2014]. SAR data was used for the mapping of geological features and paleo-landscape in different studies [Dabbagh et al., 1997; Schaber et al., 1997; Abdelsalam et al., 2000]. Subsurface paleo-drainages covered by aeolian deposits could be found with remote sensing data in Egypt, Sudan and Libya [Ghoneim and El-Baz, 2007; Rahman et al., 2010; Ghoneim et al., 2012]. The detection of edges is an essential part of the extraction of linear features from images [Quackenbush, 2004] and of digital image processing in general [Gonzalez and Woods, 2010; Nixon and Aguado, 2012]. Edge detectors are also widely used to extract linear features of SAR images. Linear objects were extracted from interferometric SAR data by applying a Markov Random Model and Bayesian classification [Hellwich et al., 2002]. A road network could be extracted from multitemporal SAR images [Chanussot et al., 1999]. Some edge detectors for SAR images consider backscatter value ratios to make them more stable against speckle noise [Touzi et al., 1988; Airouche et al., 2008]. Also Lee filters have been utilized to identify lineaments and coastlines from RADARSAT-1 and ERS-1 SAR data [Marghany and Hashim, 2010; Marghany et al., 2010]. The detection of shorelines from SAR images is a frequently applied approach [Descombes et al., 1996]. The Canny algorithm could indicate recent shoreline erosion from multitemporal SAR images [Marghany, 2002]. Niedermeier et al. [2000] used wavelets as an active contour algorithm to extract the shoreline of the German Bight. Al Fugura et al. [2011] propose a semi-automated method with several steps of filtering and noise reduction, the edge enhancement with a Sobel edge detector followed by an image segmentation. Another study utilizes the coherence information of interferometric SAR images [Dellepiane et al., 2004].

The detection and delineation of landscape forms is an important element of digital image processing in a geomorphological or geological context, as well as in archaeological and paleo-landscape studies. SAR images yield information about the physical properties (roughness and geometry) of structures and landforms. The paleo-shorelines in this case example provide no clear edges like in recent shorelines, but gradual transitions. Likewise, edge detection algorithms suffer from the SAR inherent effect of speckle noise and their effectiveness is reduced [Touzi et al., 1988]. In this case study we compare several pre-processing and filter methods combined with different edge detection techniques. The intention is to provide a benchmark for the pre-processing steps of SAR images and the selection of edge detection operators for applications dealing with landform detection.

Study area and geo-archaeological context

The endorheic Lake Manyara (954 m a.s.l.) is located in the eastern branch of the East African Rift System in northern Tanzania (Fig. 1). West of the Lake Manyara Basin is a 200 to 600 m high escarpment, whereas in the east a west dipping monocline is adjoined. The morphology of this asymmetrically shaped half graben is strongly related to Quaternary volcanism and tectonic activity, which still is active [Ring et al., 2005].

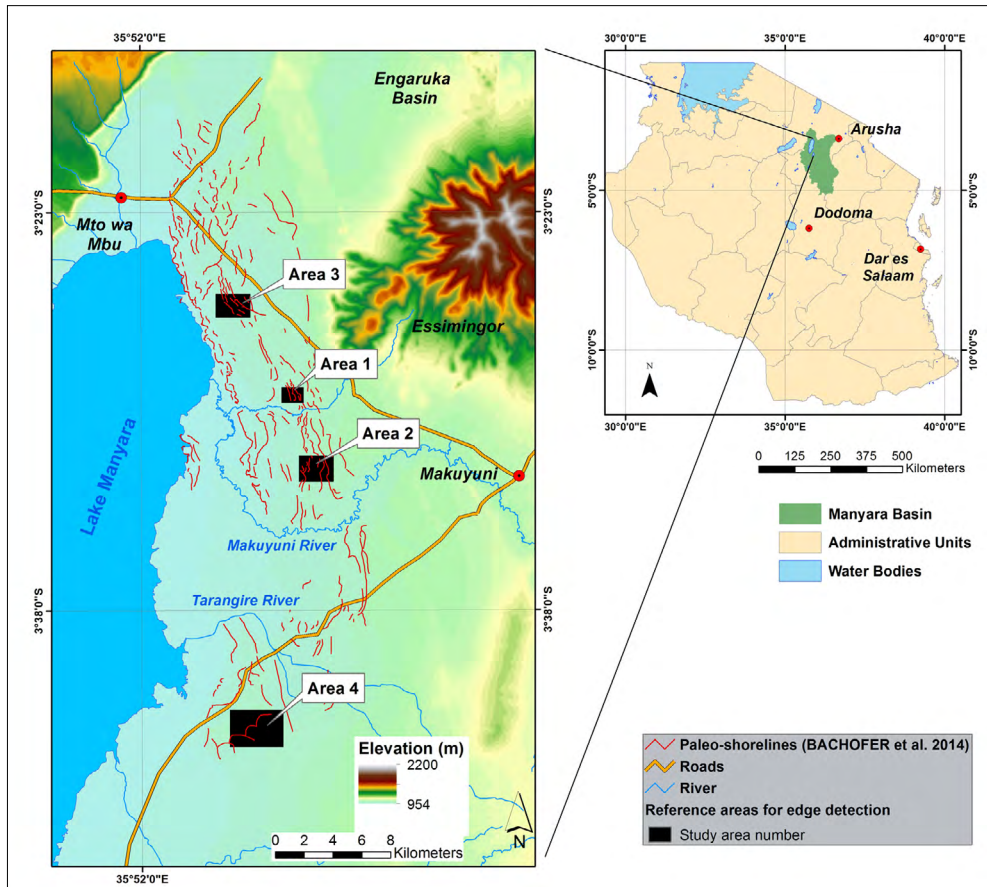


Figure 1 - Study area and test sites.

Predominantly N-S aligned paleo-shorelines occur on the monocline east of the lake. Their sizes vary from small beaches with a local relief of about 1 m to terraces which are several meters high (Fig. 2). The most prominent shorelines can be found at different elevations of 970 m, 978 m, 1002 m to 1008 m, 1018 m and 1030 m above sea level [Bachofer et al., 2014]. These paleo-shorelines were formed in more humid phases during the Quaternary when the lake level was higher. Some of these terraces consist of different levels which indicate fluctuations of the distinct paleolake levels [Keller et al., 1975]. The terraces are covered mostly with gravel sized calcrete conglomerates of up to 30 cm in diameter, which also cover the scarps. The treads are often covered by densely growing shrubs and small trees. The relatively flat areas between the terraces and beach ridges are mostly covered by young soils, which are rich in carbonate. Stromatolites, which can be found on the shorelines and within drilling cores of the lake, have been radiometrically dated [Holdship, 1976; Barker, 1990]. Humid periods with high lake levels could be identified for the following periods: 12,700 to 10,000 y BP, 22,000 y BP, 27,500 to 26,000 y BP, 27,000 to 23,000 y BP, 35,000 to 32,000 y BP, 90,000 y BP, and an uncertain age of about 140,000 y BP [Hillaire-Marcel et al., 1986; Casanova and Hillaire-Marcel, 1992].

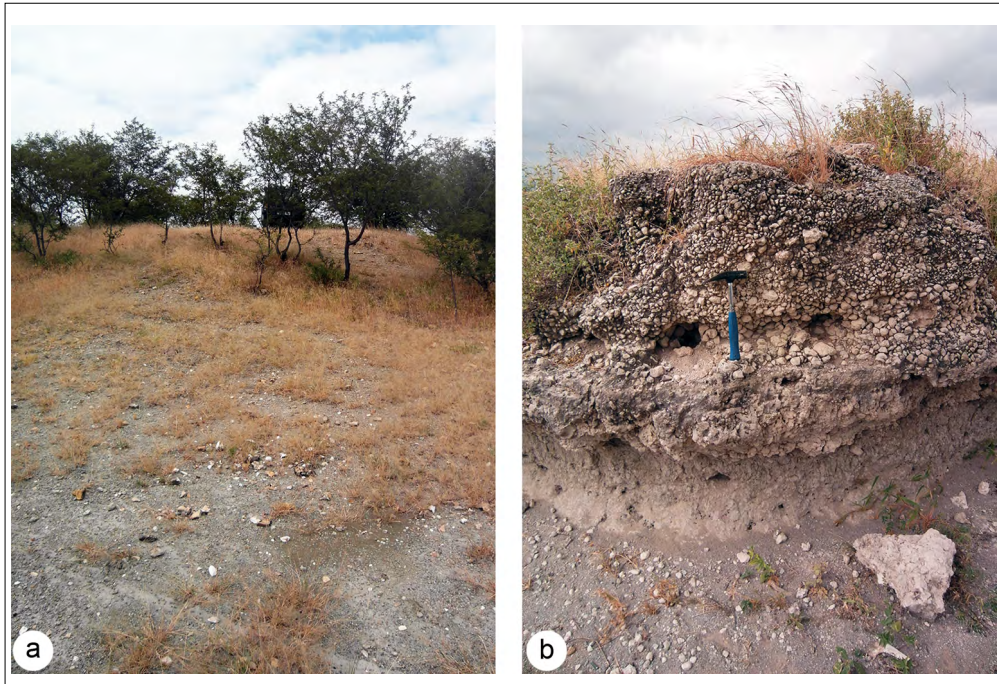


Figure 2 - (a) Distinct paleo-shoreline (Lon. 36.006°, Lat. -3.629°); (b) Shoreline section (Lon. 35.909°, Lat. -3.396°).

SAR data and processing

SAR systems illuminate a given surface and record the backscattered amplitude and the phase of the microwave signal. SAR images suffer from the speckle phenomenon which makes the interpretation and analysis difficult. It emerges as a pixel-to-pixel intensity variation. Speckle or multiplicative noise is the result of the interaction of physical properties of the ground surface and microwave signals. It is generated by the coherent addition of constructive and destructive combinations of backscatter [Lee et al., 1994; Richards, 2009]. To reduce the speckle phenomenon, multilooking and filter approaches are used with the pre-processing of the SAR data. An extensive smoothing of speckle effects leads to an information loss, a trade-off between noise reduction and information depth must therefore be determined.

SAR pre-processing

SAR sensors offer the possibility to detect and delineate distinct morphological structures. This is enabled by the relation of backscatter intensity to geometry, texture, soil moisture and surface roughness [Aubert et al., 2011; Zribi et al., 2012]. For this study we used a TerraSAR-X (TSX1) (~9.65 GHz; Single Look Complex, X-band) scene in StripMap mode. The acquisition date was 2011-09-13, 15:54 UTC (Tab 1). Soil moisture induced by precipitation leads to an increase of the dielectric constant [Aubert et al., 2011; Colliander, 2012]. The resulting increase of the backscatter intensity may reduce the

ability to discriminate between different landcover types. Even though no soil moisture measurements were available, the Tropical Rainfall Measurement Mission (TRMM) daily Rainfall Estimate product 3B42 (V7) shows no relevant precipitation for the preceding period [Huffman et al., 2007]. The TSX1 scenes were radiometrically calibrated to sigma naught (σ^0) and normalized to correct the backscatter intensity for the predominating topography using a SRTM-X DEM and the local incident angle resulting in gamma naught (γ^0) [Small et al., 2009]. The resulting images were resampled to 3 m ground resolution and normalized to a value range of [0, 1].

Table 1 - TerraSAR-X scene.

Sensor	Mode	Date	Time (UTC)	Orbit	Incident Angle	Polarization
TerraSAR-X	StripMap	2011-09-13	15:54:39	Ascending	44.4°	HH

Multilooking

Depending on the type of SAR data, there are different multilooking approaches [Lee et al., 1994; Lee and Pottier, 2009]. For the TSX1 Single Look Complex (SLC) data, multilooking averages the neighboring pixels in azimuth and slant range direction. Since the azimuth and the slant range resolution differ, multilooking is used to create square pixels. By averaging the pixels, speckle is reduced concurrently. When the number of looks is increased, the geometrical resolution is degraded.

Spatial filtering

For the comparison of filter methods to reduce speckle we utilized standard non-adaptive and adaptive filters. The non-adaptive filters do not consider local variability in an image. The median filter replaces the central pixel of a kernel with the median value of all kernel pixels, while the lowpass mean filter replaces the central pixel with the mean value of the kernel pixels. Adaptive filters consider statistical characteristics for the kernel extent [Gonzalez and Woods, 2010]. Adaptive Lee filters assume a Gaussian distribution of the noise of the pixel in a kernel. Secondly they assume a similar mean and variance of the target pixel value than for the kernel values [Lee, 1980; Touzi, 2002]. The Refined Lee filter is an improvement of the multiplicative Lee filter. In image areas with high variance the filter takes into account the orientation of supposed edges to preserve them [Lee, 1981]. The Gamma MAP (Maximum A Posteriori) filter assumes a gamma distributed cross-section and a new pixel value lying between the average kernel values and the original target pixel value. The filter thereby considers statistical and spatial properties of the image section [Frost et al., 1982; Lopes et al., 1990]. All filters were employed on the TSX1 images with a 5 x 5 kernel.

Edge detection operators

Edge detection is based on the approach that an edge is the barrier between an object and the background and additionally the boundary between overlapping objects [Dimou et al.,

2000]. In a grey-level picture containing homogeneous objects, an edge is the boundary between two regions of different grey levels [Davis, 1975].

The discrimination between two regions with intensity changes provides an estimate of the first-order derivative [Nixon and Aguado, 2012]. Template-based edge detection operators use a small, discrete template as a model of an edge instead of using a derivative operator directly [Parker, 2011]. The Roberts cross [Roberts, 1963] and Sobel [Sobel and Feldman, 1968] operators are such widely used examples. In the 1980s edge detection techniques were improved by adding preliminary filtering steps such as smoothing (most commonly with the Gaussian filter), called Laplacian of Gaussian (or Marr-Hildreth edge detector) [Marr and Hildreth, 1980]. Canny followed an approach to define edges as local maxima of the convolution of the image [Canny, 1986]. Wavelet transformation served as useful processing step for despeckling to extract edges from images [Niedermeier et al., 2000; Gleich et al., 2008].

Roberts

The Roberts edge detector performs a simple 2-D spatial gradient measurement. The operator uses a pair of 2×2 convolution kernels; one kernel is rotated by 90° . These kernels emphasize edges running at 45° to the grid, one kernel for each of the two perpendicular orientations [Maini and Aggarwal, 2009]:

$$\begin{array}{cc} 1 & 0 \\ 0 & -1 \end{array} = R_x \qquad \begin{array}{cc} 0 & 1 \\ -1 & 0 \end{array} = R_y \quad [1]$$

Sobel

The Sobel operator uses 3×3 convolution masks for the detection of the gradients x and y . Both of the kernels can be inverted, this provides four possible directions for measurements [Nixon and Aguado, 2012].

$$\begin{array}{ccc} 1 & 0 & -1 \\ 2 & 0 & -2 \\ 1 & 0 & -1 \end{array} = S_x \qquad \begin{array}{ccc} 1 & 2 & 1 \\ 0 & 0 & 0 \\ -1 & -2 & -1 \end{array} = S_y \quad [2]$$

Laplacian of Gaussian (LoG)

Marr and Hildreth [1980] combined their knowledge about biological vision into a mathematical model. The most important points are local averaging done by smoothing the image with a filter and looking for extreme values for a change in intensity (representing an edge). The most commonly used smoothing filter is the Gaussian filter. The two-dimensional Gaussian is the function being convolved with the image.

$$G_{\sigma}(x, y) = e^{-\frac{(x^2+y^2)}{2\sigma^2}} \quad [3]$$

where σ is the standard deviation of the associated Gaussian probability distribution [Parker, 2011].

After the image is convolved, the Laplacian operator ∇ can be applied:

$$\nabla^2 = \frac{\delta^2}{\delta x^2} + \frac{\delta^2}{\delta y^2} \quad [4]$$

The Laplacian has the advantage of being invariant to rotation, therefore it responds equally to changes in intensity regardless of mask direction [Gonzalez and Woods, 2010]. As the order does not matter, both, the Laplacian operator and the Gaussian filter, can be combined into the Laplacian of Gaussian (LoG):

$$\nabla^2 G_{\sigma} = \left(\frac{r^2 - 2\sigma^2}{\sigma^4} \right) e^{\left(\frac{-r}{2\sigma^2} \right)} \quad \text{where } r = \sqrt{x^2 + y^2} \quad [\text{Parker, 2011}] \quad [5]$$

Canny edge detection

Canny [1986] followed an approach to improve current methods by defining three performance criteria: i) the signal-to-noise ratio should be as large as possible, ii) the distance between the calculated edge pixels and the edge should be as small as possible and iii) the edge detector should not identify multiple edge pixels when there is one single edge. The author defined a filter that performs best for all three criteria. An efficient approximation for those criteria is the first derivative of a Gaussian function.

The Gaussian has the form:

$$G(x) = e^{-\frac{x^2}{2\sigma^2}} \quad [6]$$

The derivative with respect to x is therefore:

$$G'(x) = \left(-\frac{x}{\sigma^2} \right) e^{-\left(\frac{x^2}{2\sigma^2} \right)} \quad [7]$$

In two dimensions, a Gaussian is given by:

$$G(x, y) = \sigma^2 e^{-\left(\frac{x^2 + y^2}{2\sigma^2}\right)} \quad [8]$$

Furthermore, G has derivatives in both the x and y directions. The approximation of Canny's optimal filter for edge detection is G' , and so by convolving the input image with G' , an image E that has enhanced edges will be obtained [Parker, 2011]. The next step is a nonmaximum suppression, which suppresses all values alongside the magnitude of gradients. Hysteresis thresholding is applied to exclude weak edges which are not connected to strong edges, by tracking the edges by a lower and an upper threshold [Canny, 1986; McIlhagga, 2011].

Discrete Wavelet Transformation

The wavelet transformation developed as an advancement of the Fourier transformation in signal processing. The transformation is based on small waves (wavelets), which can have a varying frequency and are more sensitive to local variations [Mallat, 1989; Gonzalez and Woods, 2010]. They allow the decomposing of complex image information into elementary forms and the reconstruction of them again. The Discrete Wavelet Transformation (DWT), Wavelet $\psi(x)$ and scaling $\varphi(x)$ are coefficients of the function $f(x) \in L^2(\mathbf{R})$. The DWT coefficients for a sequence of numbers $f(n)$ are defined as:

$$W_\varphi(j_0, k) = \frac{1}{\sqrt{M}} \sum_n f(n) \varphi_{j_0, k}(n) \quad [9]$$

$$W_\psi(j, k) = \frac{1}{\sqrt{M}} \sum_n f(n) \psi_{j, k}(n) \quad \text{for } j \geq j_0 \quad [10]$$

The applied function results in four sub-images: the low pass approximation (LL), the low pass (rows) and high pass (columns) (vertical edge details - LH), the high pass (row) and low pass (column) (horizontal edge details - HL) and high pass filtering (diagonal edge details - HH) (Fig. 3). The reconstruction of the DWT coefficients can be achieved by:

$$f(n) = \frac{1}{\sqrt{M}} \sum_k W_\varphi(j_0, k) \varphi_{j_0, k}(n) + \frac{1}{\sqrt{M}} \sum_{j=j_0}^{\infty} \sum_k W_\psi(j, k) \psi_{j, k}(n) \quad [11]$$

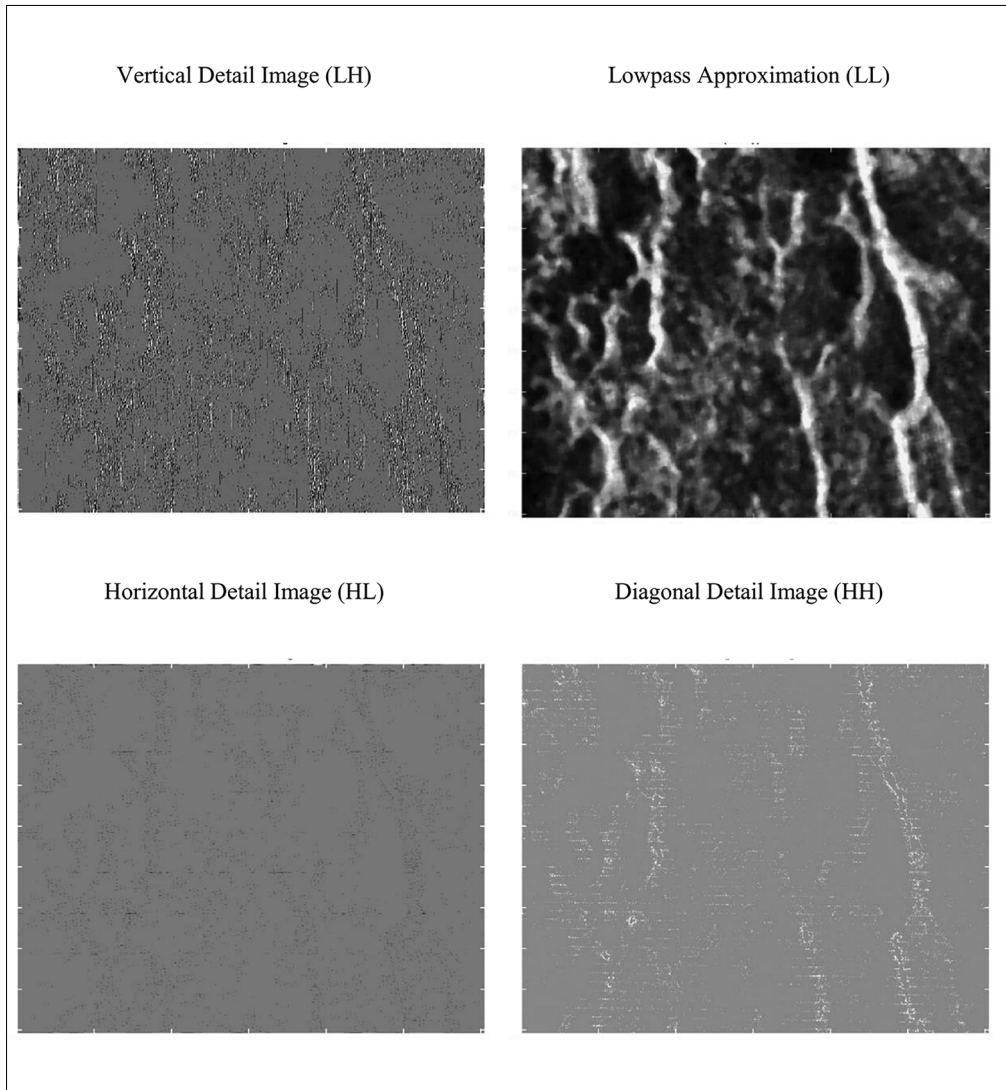


Figure 3 - One scale DWT for “test site 2” (pre-processing: multilooking 4 / median filter 5x5 kernel).

A comparison of values along a profile and a source image and the reconstructed DWT, considering three levels of decomposition, shows distinct edges where high intensities occur (Fig. 4). As operator, we used the Haar function, which is discussed in detail by Strömberg [1981] and Beylkin et al. [1991].

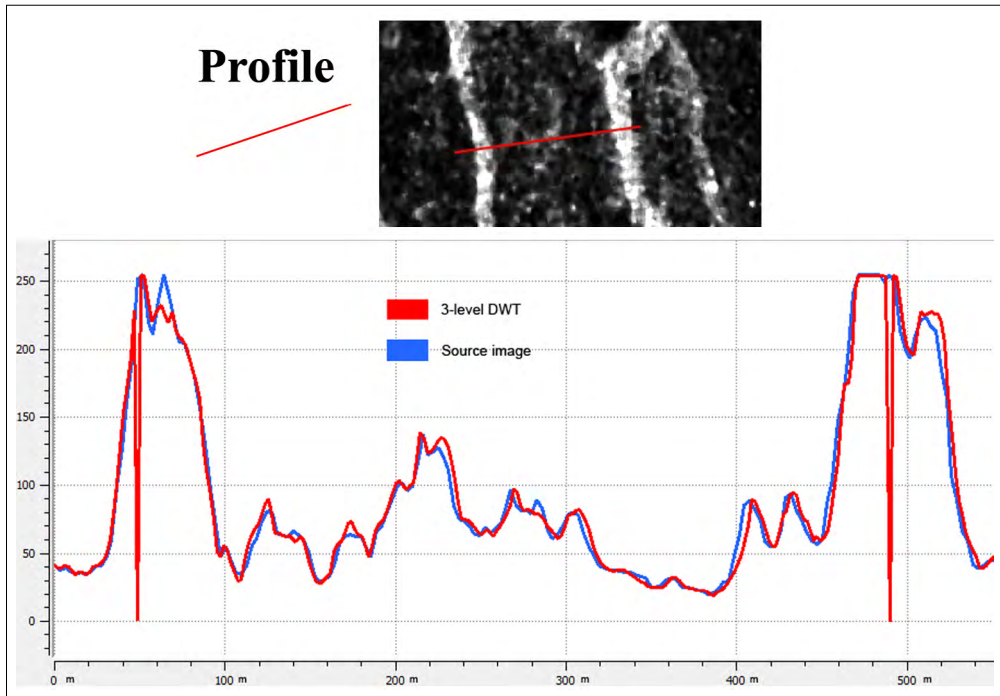


Figure 4 - Comparison of a value profile (test site 2) between source image (pre-processing: multilooking 4 / median filter 5x5 kernel) and 3-level DWT on a 520 m transect.

Experimental set-up

A different number of looks and/or one of the spatial filters were applied to the TSX-1 subsets (see Fig. 1; Area 1 to 4). The proposed edge detectors were then utilized to determine linear structures/edges in the pre-processed images. The results were compared with ground reference information which was collected by GPS tracks in the four study areas during field campaigns between 2010 and 2014 (Fig. 1). The number of edge pixels, which were identified correctly, was set into relation with wrongly identified edges in each subset. To allow the comparability of the achieved accuracies between the four test sites, the number of correctly identified pixels was normalized with the total number of pixels for each test site.

All edge detectors need at least one parameter to define a threshold, which declares a change in pixel values as an edge or a value which defines an accompanied filter. Since the selection of these values is crucial for a comparison, we applied an automated search from the upper and lower bounds of the value range, which was iteratively refined. For each study area an individual minimum number of edges to be detected were defined based on expert knowledge to assure an adequate representation of the paleo-shorelines. The Sobel and Canny Operators were applied to the reconstructed DWT in order to examine if DWT emphasizes the detection of edges of such continuous landforms.

Results and discussion

Different combinations of speckle reduction methods and edge detection algorithms were processed and compared with the corresponding field reference for each test site. The diagrams from Figure 5 illustrate the accuracies for all four study areas. Table 2 shows detailed results for a selection of processing set-ups for “study area 2”. Similar trends are recognizable in all test sites. The Canny filter outperforms all other edge detectors, with most of the pre-processing datasets, for all test sites. The results indicate that this advantage of the Canny operator is mainly achieved with a low grade pre-processing images. The first-derivative edge detectors achieve 3-6 % lower accuracies than the Canny operator for the methods with “1 look” and “2 looks” (Tab. 2, ID numbers 1 to 6). The LoG achieves lower accuracies than the other edge detectors, especially for images with a high number of looks. This is mainly because the Gaussian filter is highly affected by low gradients, which are produced with high speckle noise reduction.

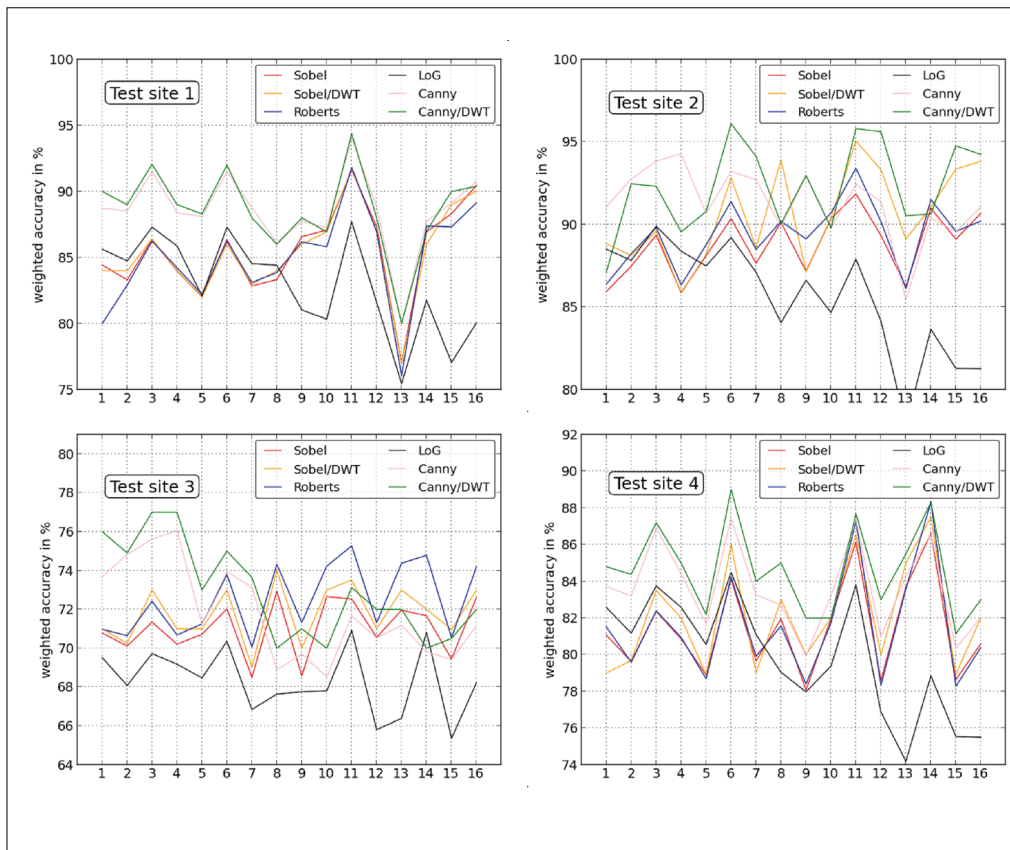


Figure 5 - Diagrams of the edge detection accuracy for the four test sites. The number on the x-axis stands for the multilooking/filter combination (see Tab. 2).

Table 2 (Continued on the next page) - Weighted accuracy in percent of edge detection methods for “test site 2”. T = threshold for edge detection; S = sigma value; LH = lower hysteresis; UH = upper hysteresis; LA = Laplacian alpha; k = kernel size.

ID / Looks / Filter	Roberts	Sobel	DWT / Sobel	LoG	Canny	DWT / Canny
(1) 1 look / no filter	86.4 % T: 0.348	85.9 % T: 0.325	88.8 % T: 0.039	88.5 % T: 0.027 S: 2	91.1 % LH/UH: 0.16 / 0.758; S: 1.5	95.0 % LH/UH: 0.152 / 0.757; S: 1.5
(2) 1 look / Lee filter (k = 5)	88.2 % T: 0.151	87.5 % T: 0.166	88.1 % T: 0.171	87.8 % T: 0.02 S: 1.8	92.7 % LH/UH: 0.112 / 0.669; S: 0.1	93.8 % LH/UH: 0.135 / 0.664; S: 0.1
(3) 1 look / median filter (k = 5)	89.8 % T: 0.175	89.4 % T: 0.183	89.6 % T: 0.186	88.4 % T: 0.02 S: 2	93.8 % LH/UH: 0.09 / 0.713; S: 0.1	94.8 % LH/UH: 0.099 / 0.706; S: 0.1
(4) 2 looks / no filter	86.3 % T: 0.22	85.9 % T: 0.239	85.8 % T: 0.261	88.4 % T: 0.026 S: 2	94.3 % LH/UH: 0.139 / 0.821; S: 0.5	94.1 % LH/UH: 0.166 / 0.815; S: 0.5
(5) 2 looks / Lee filter (k = 5)	88.8 % T: 0.068	88.1 % T: 0.081	88.2 % T: 0.081	87.5 % T: 0.011 S: 1.6	90.7 % LH/UH: 0.092 / 0.319; S: 0.5	90.8 % LH/UH: 0.086 / 0.318; S: 0.5
(6) 2 looks / median filter (k = 5)	91.4 % T: 0.074	90.4 % T: 0.085	92.8 % T: 0.093	89.2 % T: 0.012 S: 1.6	93.2 % LH/UH: 0.136 / 0.475; S: 0.1	96.1 % LH/UH: 0.049 / 0.296; S: 0.1
(7) 4 looks / no filter	88.5 % T: 0.114	87.7 % T: 0.128	88.6 % T: 0.133	87.1 % T: 0.013 S: 2.2	92.7 % LH/UH: 0.084 / 0.586; S: 0.1	94.1 % LH/UH: 0.08 / 0.481; S: 0.1
(8) 4 looks / Lee filter (k = 5)	90.2 % T: 0.031	90.1 % T: 0.037	93.9 % T: 0.045	84.1 % T: 0.005 S: 1.2	89.8 % LH/UH: 0.072 / 0.131; S: 0.1	94.4 % LH/UH: 0.108 / 0.125; S: 1.0
(9) 4 looks / refined Lee filter	89.1 % T: 0.071	87.1 % T: 0.078	87.2 % T: 0.078	86.6 % T: 0.011 S: 1.8	92.9 % LH/UH: 0.015 / 0.378; S: 0.5	93.0 % LH/UH: 0.03 / 0.377; S: 0.5
(10) 4 looks / gamma filter	90.7 % T: 0.032	90.4 % T: 0.039	90.4 % T: 0.039	90.7 % T: 0.006 S: 1.2	89.8 % LH/UH: 0.072 / 0.097; S: 0.1	89.7 % LH/UH: 0.057 / 0.105; S: 0.1

Table 2 (Continued from preceding page) - Weighted accuracy in percent of edge detection methods for “test site 2”. T = threshold for edge detection; S = sigma value; LH = lower hysteresis; UH = upper hysteresis; LA = Laplacian alpha; k = kernel size.

ID / Looks / Filter	Roberts	Sobel	DWT / Sobel	LoG	Canny	DWT / Canny
(11) 4 looks / median filter (k = 5)	93.4 % T: 0.035	91.9 % T: 0.04	95.1 % T: 0.047	87.9 % T: 0.004 S: 1.6	92.4 % LH/UH: 0.14 / 0.289; S: 0.1	95.8 % LH/UH: 0.088 / 0.189; S: 1.5
(12) 8 looks / no filter	90.2 % T: 0.047	89.3 % T: 0.056	93.3 % T: 0.065	84.1 % T: 0.004 S: 1.8	91.4 % LH/UH: 0.139 / 0.321; S: 0.1	95.6 % LH/UH: 0.089 / 0.235; S: 1
(13) 8 looks / Lee filter (k = 5)	86.1 % T: 0.018	86.3 % T: 0.023	86.1 % T: 0.026	77.8 % T: 0.001 S: 2	85.4 % LH/UH: 0.137 / 0.163; S: 0.1	90.5 % LH/UH: 0.095 / 0.24; S: 1
(14) 8 looks / median filter (k = 5)	91.5 % T: 0.022	90.9 % T: 0.026	91.1 % T: 0.026	83.7 % T: 0.001 S: 2	90.4 % LH/UH: 0.087 / 0.26; S: 0.1	90.6 % LH/UH: 0.11 / 0.258; S: 0.1
(15) 10 looks / no filter	89.6 % T: 0.038	89.1 % T: 0.047	93.4 % T: 0.054	81.3 % T: 0.002 S: 2	89.6 % LH/UH: 0.126 / 0.305; S: 0.1	94.8 % LH/UH: 0.08 / 0.17; S: 1
(16) 12 looks / no filter	90.2 % T: 0.032	90.7 % T: 0.04	93.8 % T: 0.047	81.3 % T: 0.028 S: 1	91.1 % LH/UH: 0.223 / 0.297; S: 1.5	94.2 % LH/UH: 0.063 / 0.153; S: 1.5

The performance of the Canny filter converges, with an increasing number of looks, with the accuracies of the other operators. A strong reduction in speckle noise and filtering first-order derivatives produced relative high accuracies compared to the Canny operator. Since the Canny edge detector and the LoG operator apply a filter before detecting edges, they perform relatively well with images which have a low number of looks and a relatively high share of speckle noise. This advantage declines with a further reduction of speckle noise by multilooking and spatial filtering. A balanced speckle reduction leads therewith to a significant improvement in the edge detection accuracy. For “4 looks”, “8 looks”, “10 looks” and “12 looks” (ID numbers 9 to 16) Roberts and Sobel filters perform equally well or even outperform the results of the Canny operator in certain cases.

For median filtered images, higher accuracies were achieved (ID numbers 3, 6, 11 and 14). The pre-processing chain which applied a number of “2 looks” or “4 looks” and a median filter could achieve in average the highest accuracies for all test sites and for all edge operators (ID numbers 6 and 11). Furthermore, the application of DWT leads to an improvement in the edge detection performance with up to 5 % higher accuracies.

For “test site 1” and “test site 2”, low accuracies can be found while pre-processing with

“8 looks” and Lee filtering (ID number 13). Low accuracy results for “test site 4” were produced from pre-processing with “8 looks” (ID number 12), and other pre-processing chains, where only multilooking was applied (Figs. 5 and 6). This results from a strong smoothing effect (Lee filter), which causes the borders of the shorelines to exceed the field reference and thereby significantly reduce the calculated accuracy. The same filtering yields a positive effect in “test site 4” (ID number 13, excluding LoG), whilst the images, with only multilooking and no further filtering, remain very noisy and are resulting into low accuracies (ID number 12).

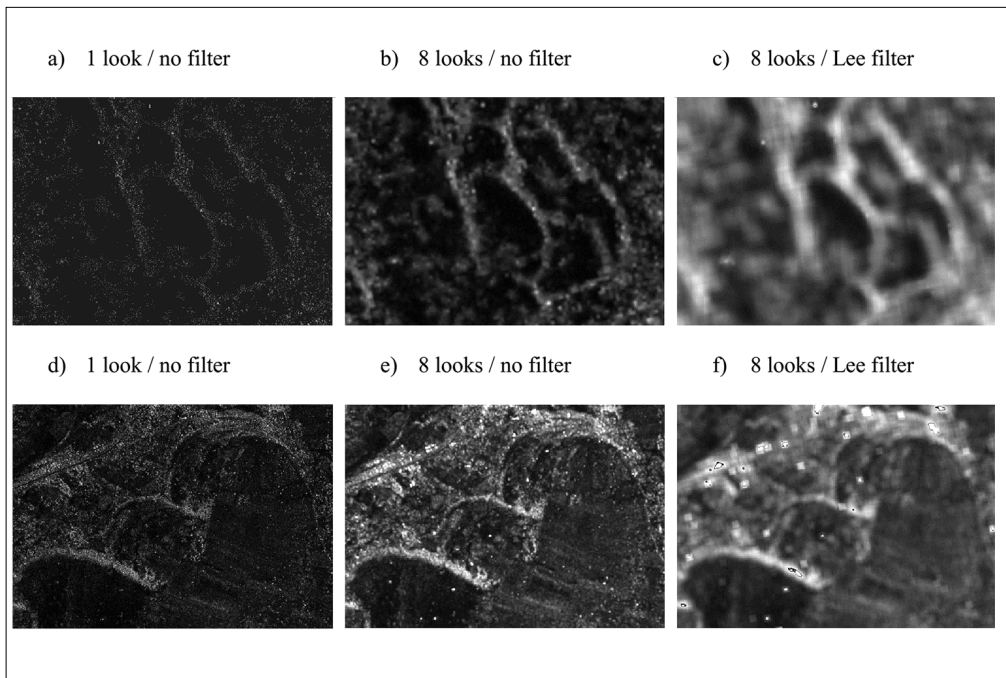


Figure 6 - Multilooking and filtering for “test site 1” (images: a, b, c with an extent of 1546 m x 1102 m) and for “test site 4” (images d, e, f with an extent of 3718 m x 1590 m).

The visual interpretation of the results for “test site 2” indicates that the Canny filter delineates the paleo-shorelines exceptionally well (Fig. 7d, k, l). While both the Sobel and the LoG operators result in many single segments, the Canny operator delivers coherent edges. First-order derivatives generally produce thicker edges in an image whereas second-order derivatives show a stronger response to thin lines and noise. The DWT reduces the number of artifacts and amplifies the target structures significantly.

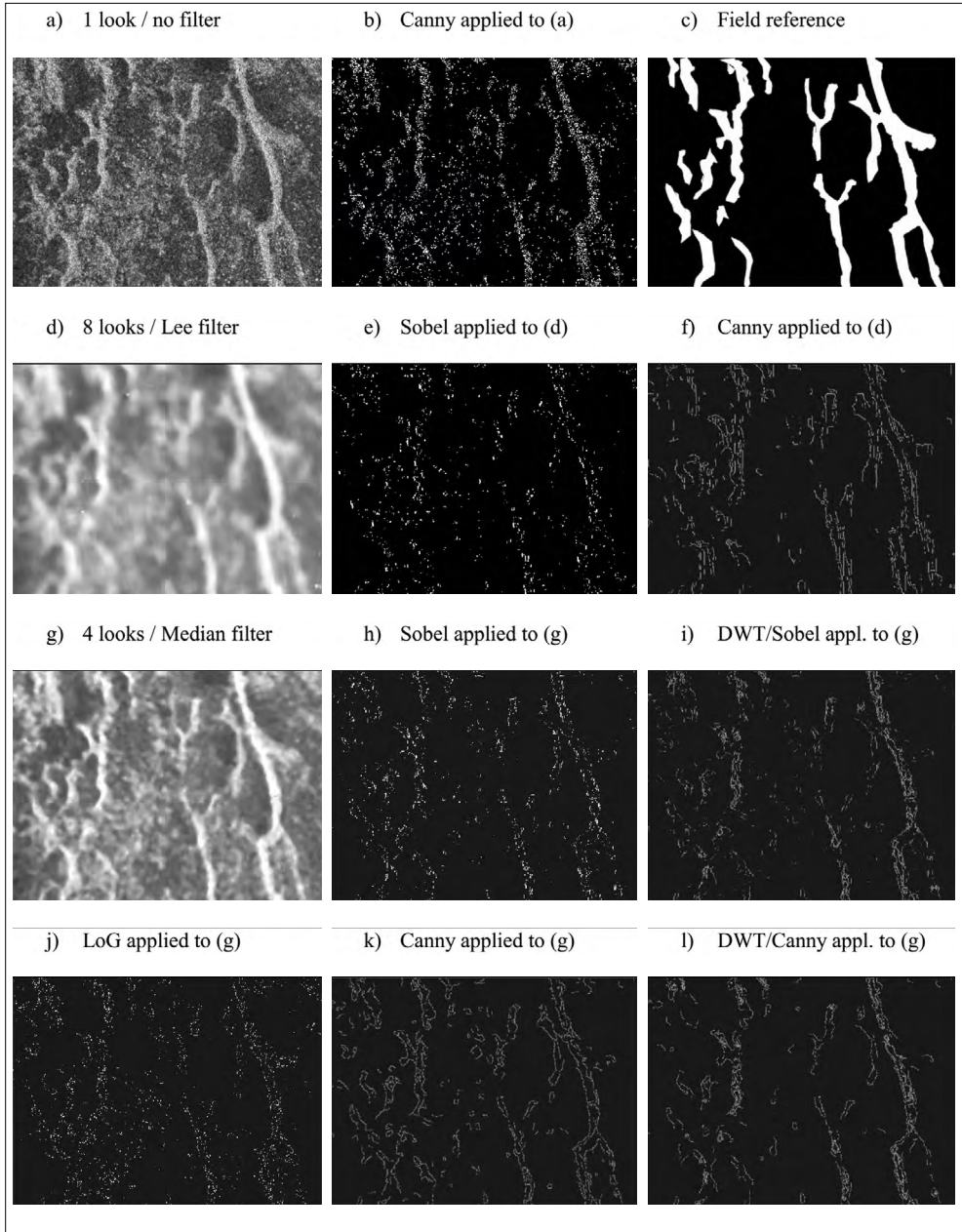


Figure 7 - Speckle reduction and edge detection for “study area 2”. The extent of the image is 2400 m x 1800 m. a), d) and g) represent different pre-processing examples.

Conclusions

In conclusion, the study has demonstrated that by using edge detectors, morphological features in SAR images can be detected with high accuracies. We compared different

speckle reduction techniques in combination with different edge detectors, striving to detect paleo-shorelines in a TSX1 SAR image. The case study determined that the performance of the proposed pre-processing techniques and edge detectors lead to different accuracies. The Canny edge detector is especially suitable for images exhibiting a high speckle noise. The combination of DWT and the Canny operator yields the highest accuracies and provides stable results with different pre-processing steps. First-derivative edge operators have proven to perform well when applied to speckle reduced images. Median filtering proved to be an advantageous pre-processing step.

We are inclined to state that the derived values for thresholds of the operators and the lower and upper hysteresis of the canny operator are dependent on the land cover, soil moisture, and morphological structure of the target features, as well as the wavelength and the calibration of the SAR sensor. Nevertheless, the general trend in the results can be transferred to other edge detection issues and serves as a benchmark.

Acknowledgments

This study was financed by the Heidelberg Academy of Sciences and Humanities research center: “The Role of Culture in Early Expansions of Humans” (ROCEEH). We would like to thank the DLR and the German Remote Sensing Data Center (DFS) for providing the TerraSAR-X and the SRTM/X-SAR data. We acknowledge support by Deutsche Forschungsgemeinschaft and Open Access Publishing Fund of Tuebingen University.

References

- Abdelsalam M.G., Robinson C., El-Baz F., Stern R.J. (2000) - *Application of Orbital Imaging Radar for Geologic Studies in Arid Regions: The Saharan Testimony*. Photogrammetric Engineering & Remote Sensing, 66 (6): 717-726.
- Airouche M., Zelmat M., Kidouche M. (2008) - *Statistical Edge Detectors Applied to SAR Images*. International Journal of Computers Communications & Control, 3: 144-149.
- Al Fugura A.K., Billa L., Pradhan B. (2011) - *Semi-automated procedures for shoreline extraction using single RADARSAT-1 SAR image*. Estuarine, Coastal and Shelf Science, 95 (4): 395-400. doi: <http://dx.doi.org/10.1016/j.ecss.2011.10.009>.
- Aubert M., Baghdadi N., Zribi M., Douaoui A., Loumagne C., Baup F., El Hajj M., Garrigues S. (2011) - *Analysis of TerraSAR-X data sensitivity to bare soil moisture, roughness, composition and soil crust*. Remote Sensing of Environment, 115 (8): 1801-1810. doi: <http://dx.doi.org/10.1016/j.rse.2011.02.021>.
- Bachofer F., Quénéhervé G., Märker M. (2014) - *The Delineation of Paleo-Shorelines in the Lake Manyara Basin Using TerraSAR-X Data*. Remote Sensing, 6 (3): 2195-2212. doi: <http://dx.doi.org/10.3390/rs6032195>.
- Barker P.A. (1990) - *Diatoms as palaeolimnological indicators: A reconstruction of Late Quaternary environments in two East African salt lakes*. Loughborough University of Technology, Dissertation, 267 pp.
- Beylkin G., Coifman R., Rokhlin V. (1991) - *Fast wavelet transforms and numerical algorithms I*. Communications on Pure and Applied Mathematics, 44 (2): 141-183. doi: <http://dx.doi.org/10.1002/cpa.3160440202>.
- Canny J. (1986) - *A Computational Approach to Edge Detection*. IEEE Transactions on Pattern Analysis and Machine Intelligence, PAMI-8 (6): 679-698. doi: <http://dx.doi.org/10.1109/34.223818>.

- org/10.1109/TPAMI.1986.4767851.
- Casanova J., Hillaire-Marcel C. (1992) - *Chronology and paleohydrology of late Quaternary high lake levels in the Manyara basin (Tanzania) from isotopic data (18O, 13C, 14C, ThU) on fossil stromatolites*. Quaternary Research, 38 (2): 205-226. doi: [http://dx.doi.org/10.1016/0033-5894\(92\)90057-P](http://dx.doi.org/10.1016/0033-5894(92)90057-P).
- Chanussot J., Mauris G., Lambert P. (1999) - *Fuzzy fusion techniques for linear features detection in multitemporal SAR images*. IEEE Transactions on Geoscience and Remote Sensing, 37 (3): 1292-1305. doi: <http://dx.doi.org/10.1109/36.763290>.
- Colliander A. (2012) - *Analysis of coincident L-band radiometer and radar measurements with respect to soil moisture and vegetation conditions*. European Journal of Remote Sensing, 45: 111-120. doi: <http://dx.doi.org/10.5721/EuJRS20124511>.
- Dabbagh A.E., Al-Hinai K.G., Asif Khan M. (1997) - *Detection of sand-covered geologic features in the Arabian Peninsula using SIR-C/X-SAR data*. Remote Sensing of Environment, 59 (2): 375-382. doi: [http://dx.doi.org/10.1016/S0034-4257\(96\)00160-5](http://dx.doi.org/10.1016/S0034-4257(96)00160-5).
- Davis L.S. (1975) - *A survey of edge detection techniques*. Computer Graphics and Image Processing, 4: 248-270. doi: [http://dx.doi.org/10.1016/0146-664X\(75\)90012-X](http://dx.doi.org/10.1016/0146-664X(75)90012-X).
- Dellepiane S., De Laurentiis R., Giordano F. (2004) - *Coastline extraction from SAR images and a method for the evaluation of the coastline precision*. Pattern Recognition Letters, 25 (13): 1461-1470. doi: <http://dx.doi.org/10.1016/j.patrec.2004.05.022>.
- Descombes X., Moctezuma M., Maître H., Rudant J.-P. (1996) - *Coastline detection by a Markovian segmentation on SAR images*. Signal Processing, 55 (1): 123-132. doi: [http://dx.doi.org/10.1016/S0165-1684\(96\)00125-9](http://dx.doi.org/10.1016/S0165-1684(96)00125-9).
- Dimou A., Uzunoglou N., Frangos P., Jäger G., Benz U. (2000) - *Linear features detection in SAR images using Fuzzy Edge Detector*. Proceedings of SBOT 2000, Samos/Greece, 49: 1-12.
- Elmahdy S.I. (2012) - *Hydromorphological Mapping and Analysis for Characterizing Darfur Paleolake, NW Sudan Using Remote Sensing and GIS*. International Journal of Geosciences, 2012 (3): 25-36. doi: <http://dx.doi.org/10.4236/ijg.2012.31004>.
- Frost V.S., Stiles J.A., Shanmugan K.S., Holtzman J. (1982) - *A Model for Radar Images and Its Application to Adaptive Digital Filtering of Multiplicative Noise*. IEEE Transactions on Pattern Analysis and Machine Intelligence, PAMI-4 (2): 157-166. doi: <http://dx.doi.org/10.1109/TPAMI.1982.4767223>.
- Gaber A., Ghoneim E., Khalaf F., El-Baz F. (2009) - *Delineation of paleolakes in the Sinai Peninsula, Egypt, using remote sensing and GIS*. Journal of Arid Environments, 73 (1): 127-134. doi: <http://dx.doi.org/10.1016/j.jaridenv.2008.08.007>.
- Ghoneim E., Benedetti M., El-Baz F. (2012) - *An integrated remote sensing and GIS analysis of the Kufrah Paleoriver, Eastern Sahara*. Geomorphology, 139-140 (0): 242-257. doi: <http://dx.doi.org/10.1016/j.geomorph.2011.10.025>.
- Ghoneim E., El-Baz F. (2007) - *The application of radar topographic data to mapping of a mega-paleodrainage in the Eastern Sahara*. Journal of Arid Environments, 69 (4): 658-675. doi: <http://dx.doi.org/10.1016/j.jaridenv.2006.11.018>.
- Ghoneim E., El-Baz F. (2007) - *DEM-optical-radar data integration for palaeohydrological mapping in the northern Darfur, Sudan: implication for groundwater exploration*. International Journal of Remote Sensing, 28 (22): 5001-5018. doi: <http://dx.doi.org/10.1080/01431160701266818>.

- Gleich D., Kseneman M., Datcu M. (2008) - *Despeckling of TerraSAR-X data using second generation wavelets*. ESA-EUSC 2008, Image Information Mining: pursuing automation of geospatial intelligence for environment and security, Frascati (Italy).
- Gonzalez R.C., Woods R.E. (2010) - *Digital image processing*. 3rd, Prentice Hall, Upper Saddle River, N.J.
- Hellwich O., Laptev I., Mayer H. (2002) - *Extraction of linear objects from interferometric SAR data*. International Journal of Remote Sensing, 23 (3): 461-475. doi: <http://dx.doi.org/10.1080/01431160110046750>.
- Hillaire-Marcel C., Carro O., Casanova J. (1986) - *14C and ThU dating of Pleistocene and Holocene stromatolites from East African paleolakes*. Quaternary Research, 25 (3): 312-329. doi: [http://dx.doi.org/10.1016/0033-5894\(86\)90004-9](http://dx.doi.org/10.1016/0033-5894(86)90004-9).
- Holdship S.A. (1976) - *The paleolimnology of Lake Manyara, Tanzania : a diatom analysis of a 56 meter sediment core: a diatom analysis of a 56 meter sediment core*. Duke University, Dissertation, 133 pp.
- Huffman G.J., Adler R.F., Bolvin D.T., Gu G.J., Nelkin E.J., Bowman K.P., Hong Y., Stocker E.F., Wolff D.B. (2007) - *The TRMM multisatellite precipitation analysis (TMPA): Quasi-global, multiyear, combined-sensor precipitation estimates at fine scales*. Journal of Hydrometeorology, 8 (1): 38-55. doi: <http://dx.doi.org/10.1175/JHM560.1>.
- Keller C.M., Hansen C., Alexander C.S. (1975) - *Archaeology and Paleoenvironments in the Manyara and Engaruka Basins, Northern Tanzania*. Geographical Review, 65 (3): 364-376. doi: <http://dx.doi.org/10.2307/213535>.
- Lee J.-S. (1981) - *Refined filtering of image noise using local statistics*. Computer Graphics and Image Processing, 15 (4): 380-389. doi: [http://dx.doi.org/10.1016/S0146-664X\(81\)80018-4](http://dx.doi.org/10.1016/S0146-664X(81)80018-4).
- Lee J.-S., Pottier E. (2009) - *Polarimetric radar imaging : from basics to applications*. CRC Press, Boca Raton, Fla. doi: <http://dx.doi.org/10.1201/9781420054989>.
- Lee J.S. (1980) - *Digital image enhancement and noise filtering by use of local statistics*. IEEE Transactions on Pattern Analysis and Machine Intelligence, 2 (2): 165-168. doi: <http://dx.doi.org/10.1109/TPAMI.1980.4766994>.
- Lee J.S., Jurkevich L., Dewaele P., Wambacq P., Oosterlinck A. (1994) - *Speckle filtering of synthetic aperture radar images: A review*. Remote Sensing Reviews, 8 (4): 313-340. doi: <http://dx.doi.org/10.1080/02757259409532206>.
- Lopes A., Nezry E., Touzi R., Laur H. (1990) - *Maximum a posteriori speckle filtering and first order texture models in SAR images*. 10th Annual International of Geoscience and Remote Sensing Symposium, Remote Sensing Science for the Nineties, pp. 2409-2412. doi: <http://dx.doi.org/10.1109/IGARSS.1990.689026>.
- Maini R., Aggarwal H. (2009) - *Study and Comparison of Various Image Edge Detection Techniques*. International Journal of Image Processing, 3 (1): 1-11.
- Mallat S.G. (1989) - *A theory for multiresolution signal decomposition: the wavelet representation*. IEEE Transactions on Pattern Analysis and Machine Intelligence, 11 (7): 674-693. doi: <http://dx.doi.org/10.1109/34.192463>.
- Marghany M. (2002) - *Operational of Canny Algorithm on SAR data for modelling shoreline change*. Photogrammetrie, Fernerkundung, Geoinformation, 2: 93-102.
- Marghany M., Hashim M. (2010) - *Developing adaptive algorithm for automatic detection of geological linear features using RADARSAT-1 SAR data*. International Journal of

- Physical Sciences, 5: 2223-2229.
- Marghany M., Sabu Z., Hashim M. (2010) - *Mapping coastal geomorphology changes using synthetic aperture radar data*. International Journal of Physical Sciences, 5 (12): 1890-1896.
- Marr D., Hildreth E. (1980) - *Theory of Edge Detection*. Proceedings of the Royal Society of London. Series B. Biological Sciences, 207 (1167): 187-217. doi: <http://dx.doi.org/10.1098/rspb.1980.0020>.
- McIlhagga W. (2011) - *The Canny Edge Detector Revisited*. International Journal of Computer Vision, 91 (3): 251-261. doi: <http://dx.doi.org/10.1007/s11263-010-0392-0>.
- Niedermeier A., Romaneessen E., Lehner S. (2000) - *Detection of coastlines in SAR images using wavelet methods*. IEEE Transactions on Geoscience and Remote Sensing, 38 (5): 2270-2281. doi: <http://dx.doi.org/10.1109/36.868884>.
- Nixon M.S., Aguado A.S. (2012) - *Feature extraction & image processing for computer vision*. 3rd, Academic Press, Oxford.
- Parker J.R. (2011) - *Algorithms for image processing and computer vision*. 2nd, Wiley Computer Pub., New York.
- Quackenbush L.J. (2004) - *A Review of Techniques for Extracting Linear Features from Imagery*. Photogrammetric Engineering & Remote Sensing, 70 (12): 1383-1392. doi: <http://dx.doi.org/10.14358/PERS.70.12.1383>.
- Rahman M.M., Tetuko Sri Sumantyo J., Sadek M.F. (2010) - *Microwave and optical image fusion for surface and sub-surface feature mapping in Eastern Sahara*. International Journal of Remote Sensing, 31 (20): 5465-5480. doi: <http://dx.doi.org/10.1080/01431160903302999>.
- Richards J.A. (2009) - *Remote sensing with imaging radar*. Springer, Heidelberg, New York. doi: <http://dx.doi.org/10.1007/978-3-642-02020-9>.
- Ring U., Schwartz H.L., Bromage T.G., Sanaane C. (2005) - *Kinematic and sedimentological evolution of the Manyara Rift in northern Tanzania, East Africa*. Geological Magazine, 142 (4): 355-368. doi: <http://dx.doi.org/10.1017/S0016756805000841>.
- Roberts, L.G. (1963) - *Machine perception of three-dimensional solids*. Massachusetts Institute of Technology. Department of Electrical Engineering, Massachusetts Institute of Technology, Dissertation
- Schaber G.G., McCauley J.F., Breed C.S. (1997) - *The use of multifrequency and polarimetric SIR-C/X-SAR data in geologic studies of Bir Safsaf, Egypt*. Remote Sensing of Environment, 59 (2): 337-363. doi: [http://dx.doi.org/10.1016/S0034-4257\(96\)00143-5](http://dx.doi.org/10.1016/S0034-4257(96)00143-5)
- Small D., Miranda N., Meier E. (2009) - *A revised radiometric normalisation standard for SAR*. IEEE International Symposium of Geoscience and Remote Sensing, 4, IV-566-IV-569. doi: <http://dx.doi.org/10.1109/igarss.2009.5417439>.
- Sobel I., Feldman G. (1968) - *A 3x3 Isotropic Gradient Operator for Image Processing*. Presented at a talk at the Stanford Artificial Project.
- Somi E.J. (1993) - *Paleoenvironmental Changes in Central and Coastal Tanzania During the Upper Cenozoic: Magnetostratigraphy, Sedimentary Records and Shorelevel Changes*. Department of Geology and Geochemistry, Paleogeophysics & Geodynamics, University of Stockholm, Dissertation, 100 pp.
- Strömberg J. (1981) - *A modified Haar system and higher order spline systems on R as unconditional bases for Hardy spaces*. Conference in Harmonic Analysis in Honor of

Antoni Zygmund II, 475-493, Belmont, California, USA.

Touzi R. (2002) - *A review of speckle filtering in the context of estimation theory*. IEEE Transactions on Geoscience and Remote Sensing, 40 (11): 2392-2404. doi: <http://dx.doi.org/10.1109/TGRS.2002.803727>.

Touzi R., Lopes A., Bousquet P. (1988) - *A statistical and geometrical edge detector for SAR images*. IEEE Transactions on Geoscience and Remote Sensing, 26 (6): 764-773. doi: <http://dx.doi.org/10.1109/36.7708>.

Zribi M., Kotti F., Lili-Chabaane Z., Baghdadi N., Ben Issa N., Amri R., Duchemin B., Chehbouni A. (2012) - *Soil Texture Estimation Over a Semiarid Area Using TerraSAR-X Radar Data*. IEEE Geoscience and Remote Sensing Letters, 9 (3): 353-357. doi: <http://dx.doi.org/10.1109/LGRS.2011.2168379>.

© 2016 by the authors; licensee Italian Society of Remote Sensing (AIT). This article is an open access article distributed under the terms and conditions of the Creative Commons Attribution license (<http://creativecommons.org/licenses/by/4.0/>).